Fracture and Failure Behavior of Partially Consolidated Discontinuous Glass Fiber Mat-Reinforced Polypropylene Composites (Azdel SuperLite®)

*Oleg Benevolenski, József Karger-Kocsis**

Institut für Verbundwerkstoffe GmbH, Universität Kaiserslautern, POBox 3049
D-67653 Kaiserslautern, Germany

Summary: The fracture and failure behavior of partially consolidated discontinuous glass fiber (GF) mat reinforced thermoplastic polypropylene (Azdel SuperLite®) composite sheets of various densities (0.35, 0.5 and 0.7 $g \cdot cm^{-3}$) but with the same amount of GF (55 wt.%) were studied under static (in-plane) and dynamic (out-of-plane perforation impact) conditions. The fracture toughness (K_Q) determined on single edge notched static tensile loaded (SEN-T) specimens, increased with increasing density (or surface weight as the sheet thickness was constant, viz. 2 mm). Location of the acoustic emission (AE) and mapping the temperature rise during loading of the SEN-T specimens via infrared thermography (IT) served to estimate the damage zone and trace the crack advance. Both techniques seem to be promising tools to determine the energy release rate directly. The unexpected high K_Q value was attributed to a combined effect of fiber nesting (achieved by the papermaking production technology) and high stress transfer GF length (owing to partial consolidation). This resulted in an efficient stress transfer and stress redistribution during damage zone development and growth. The resistance to perforation impact of the SuperLite® sheets also increased with their density (surface weight).

1. Introduction

Glass fiber mat-reinforced thermoplastic polypropylene (GMT-PP) composites are widely used as structural parts, especially in the automotive industry[1)]. Recently, GMT-PPs are strongly challenged by long discontinuous glass fiber reinforced thermoplastics produced by direct (on-line) compounding[2)]. The mat constituent of GMT-PPs is either continuous- (swirl) or discontinuous-type (needled, deposited web)[2-4)]. The latter type GMT-PP can be produced by slurry deposition (papermaking technology) using chopped PP fibers or PP powders. This technique is practiced among others by the Azdel Co. Until recently, efforts were focused on how to achieve a complete consolidation of the GMT-PP preforms, which are usually processed by compression flow molding. This step is, however, not necessary for some lightweight sheet applications requiring improved flexural resistance, such as automotive

 CCC 1022-1360/00/$ 17.50+.50/0

ceiling covers. Note that even partially consolidated GMT-PP sheets may have rather high flexural stiffness and strength values, as they are proportional with the 2nd and the 3rd power of thickness, respectively. Albeit partially consolidated GMT-PP can be produced also on melt impregnation lines (via chemical or physical foaming, exploiting the lofting phenomenon), this is a more straightforward task for papermaking processes producing wet laid, non-consolidated webs with discontinuous GF mat. Fig. 1 depicts the scheme of the manufacturing of Azdel SuperLite® (SL) sheets[5]. This process is very versatile as both the GF content and the consolidation degree can be tailored upon request. The result is a partially consolidated GMT-PP sheet with chopped GF mat reinforcement showing various densities (surface weights).

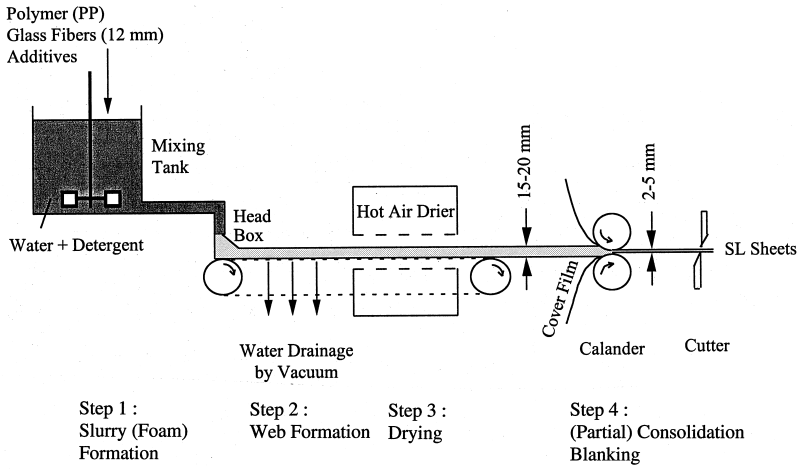

Fig. 1: Scheme of the production line of partially consolidated discontinuous GF mat-reinforced PP sheets (Azdel SuperLite®)[5].

In contrast to fully consolidated GMT-PPs of similar layout less information is available on the partially consolidated versions, which show a pronounced market penetration. Nevertheless, it is highly challenging to figure out the analogies and discrepancies between partially and fully consolidated GMT-PPs. This study was focused on the in- and out-of-plane fracture behavior of partially consolidated Azdel SL sheets of varying density. A further aim was to get a deeper understanding on the damage characteristics and failure mode in partially consolidated GMT-PP. This required a refined treatment of the results of the acoustic emission (AE) and Infrared Thermography (IT), which are well-established tools for damage and failure detection in GMT-PP.

2. Experimental

2.1. Materials

Partially consolidated Azdel SuperLite® sheets of 2 mm thickness and of various densities, viz. 0.35, 0.5 and 0.7 g·cm^{-3}, were kindly provided by Azdel BV, Bergen op Zoom, The Netherlands. The GF content of the sheets having 700, 1000 and 1400 g·m^{-2} surface weights was identical (55 wt.%). The latter data were proved by density measurements and ashing, respectively. The average length of the discontinuous GFs was 12 mm. The designation introduced for the sheets in this paper is as follows: SL denoting SuperLite, followed by the surface weight.

2.2. Tests

Flexural Tests

Dynamic-mechanical thermal analysis (DMTA) was performed on rectangular specimens of 20 mm width in 3 point bending using an Eplexor 150N device of Gabo Qualimeter. The static and sinusoidal oscillating load at 10 Hz frequency was set for 4 and ±2 N, respectively. The complex flexural modulus (E^*) and its constituents and the mechanical loss factor (tgδ) were evaluated in a temperature range from -50°C up to final failure using a heating rate of 1 °C·min^{-1}. The upper temperature threshold strongly depended on the density of the samples under the loading conditions selected.

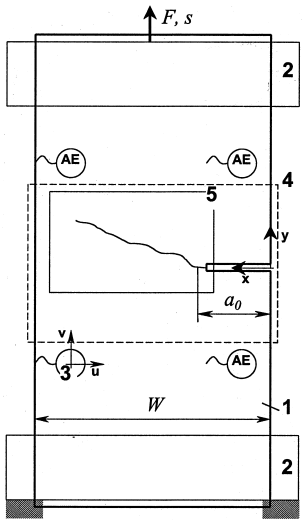

Fig. 2: Experimental set-up including dimensions of SEN-T specimen, position of the AE sensors and coordinate systems.
Designations:
1 – SEN-T specimen (W=70mm, a_0=20mm),
2 – grips,
3 – square array of 4 AE sensors,
4 – IR camera window,
5 – zoom window around crack pattern.

In-Plane Static Loading and Related Failure

Single-edge notched specimens (Fig. 2) were tensile loaded (SEN-T) on a Zwick universal testing machine at room temperature and 1 mm·min^{-1} crosshead speed. The fracture toughness (K_Q - this designation implies that this is not the critical plane strain value) was computed by considering the maximum tensile force F and terms related to the SEN-T configuration (cf. Fig. 2):

$$K_Q = f(a/W) \cdot \frac{F}{b\sqrt{W}}, \tag{1}$$

where W – the specimen width, a – the total notch length (produced by saw and razor blade; ca. 20 mm), and $f(a/W)$ – geometry related factor[6]. The AE activity was recorded in-situ by a Defektophone NEZ 220 device (AEKI, Budapest, Hungary). A four sensor quadratic array, as indicated in Fig. 2, served to locate the AE events using wide bandwidth microsensors (10 mm diameter, Micro-30D of Physical Acoustic Corporation). Location occurred in the ***uv*** coordinate system by a built-in algorithm based on the acoustic wave speed determined previously (1550 m·s^{-1}, 2000 m·s^{-1} and 2650 m·s^{-1} for SL 700, SL 1000 and SL 1400 respectively). For the damage evaluation the ***xy*** coordinate system, shown in Fig. 2, was used. Both time- (measured burst type AE signal parameters) and frequency-domain characteristics (not reported in this paper) were collected. The measured area under the rectified signal envelope (MARSE), further referred as AE energy or E_{AE}, was calculated for each AE signal according to Equation (2):

$$E_{AE} = t_w \frac{A - A_T}{\ln A - \ln A_T}, \tag{2}$$

where A – signal amplitude, A_T – preset threshold and t_w – signal duration (or width). The threshold A_T was 33.7 μV in this case. Mapping of the located AE energy over the specimen surface (guarded by the array of the AE sensors) was done by cumulating the AE energy values at identical discrete positions for the entire fracture process as well as for specific time intervals via a home written Visual Basic for Applications program implemented in Microsoft Excel.

Smoothing of the AE energy mapping was performed by weighted averaging[7] of energy over a spatial neighborhood of each point **x** in a domain S:

$$\overline{f}(\mathbf{x}) = \int_S \alpha(\mathbf{x},\xi) f(\xi) d\xi \,, \tag{3}$$

where $f(\mathbf{x})$ stands for original AE energy mapping and $\alpha(\mathbf{x},\xi)$ is the weighting function. The weighting function α was a bell-shaped function applied for the distance $r = |\mathbf{x} - \xi|$ (cf. Equation 4). The largest distance of point ξ affecting the average at point **x,** and called interaction radius R, was set to 3 mm. At the vicinity of boundaries the weighting function was rescaled not to alter a uniform field.

$$\alpha(r) = \begin{cases} (1 - \dfrac{r^2}{R^2}) & \text{if} \quad 0 \le r \le R \\ 0 & \text{if} \quad r \le R \end{cases} \tag{4}$$

Movement of *AE energy intensity peak* (further referred as *AE peak*) was traced according to the following algorithm. The entire AE history was subdivided into subsequent, not intersecting intervals starting from the first event. Each of them accounted approximately 10 μV·s cumulative AE energy. The position of the AE peak was determined according to the weight center rule, where AE energy at each point was regarded as its gravity. An average time was obtained by considering the beginning and the end of the respective time interval. Related AE peak position was rendered to the above average time.

The temperature rise during tensile loading of the SEN-T specimens was followed also in-situ by an IT camera (Compact Thermo TVS 200). IT frames were saved at selected points of the loading (each 11-12 seconds) to floppy disks and served further for digital processing. In addition, the IT map was videotaped simultaneously. Relative temperature distribution ΔT of the view field was obtained by relating the respective measured temperature field to that of in the beginning of the measurement (Frame 0). This was done based on zoomed windows (see Fig. 2). A bilinear interpolation with averaging over the neighboring values was applied to the temperature field in order to decrease the noise.

The released heat per surface unit was estimated by Equation (5) in which the heat loss during the measurement was neglected:

$$\frac{\partial \mathrm{E}_{\mathrm{IT}}}{\partial x \partial y} = \rho \cdot b \cdot c_p \cdot \Delta T(x, y) \,, \tag{5}$$

where ρ – mass density, b – specimen thickness, c_p – heat capacity defined according to the mixture rule from the tabulated heat capacities of the constituents. Recall that according to Equitation (5) c_p is constant, i.e. the effect of entrapped air is neglected.

Out-of-Plane Perforation Impact

Quadratic specimens of 70x70 mm^2 surface were cut of the sheets and subjected to instrumented falling weight impact (IFWI). The clamped diameter was 40 mm. The speed of the indenter with an instrumented hemispherical tip of diameter 13 mm was 4 $m \cdot s^{-1}$, the incident impact energy was 25.74 J. IFWI fractograms were recorded by a Dartvis device of Ceast (Pianezza, Italy), however for the data evaluation a non-commercial software was used. From the IFWI traces the following data were read or computed:

- at the maximum load (F_{peak}): deflection (X_{peak}), energy (E_{peak}), maximum strength ($\sigma_{max} = 2.5 \cdot F_{peak}/t^2$);
- at the perforation: deflection (X_{tot}), energy (E_{tot}).

For characterization of the overall failure the ductility index (DI) was considered – $DI=(E_{tot}-E_{peak})/E_{tot}$. The force and energy values were customarily normalized to the thickness, as this normalization is helpful for a direct comparison with fully consolidated GMT-PPs. Based on previous experience[8] a low pass filter with the cutoff frequency at 1.5 kHz was applied for the fractograms.

To study the failure behavior macro photographs were taken on the fracture surface of the specimens.

3. Results and Discussions

3.1. Dynamic-Mechanical Thermal Analysis (DMTA)

Fig. 3 shows the absolute value of the complex flexural modulus as a function of temperature for the SL sheets tested. One can notice that the flexural stiffness strongly increased with increasing density as expected. The density is likely controlling the thermal resistance of the sheets. The mechanical loss factor (tgδ) vs. temperature curves display clearly the degree of consolidation of SL. Note that the higher tgδ, the lower is the consolidation degree represented by the density. In the tgδ-T curves the β-relaxation or glass transition (T_g) of PP can well be observed at ambient temperature especially for the sheets of high surface weights (densities).

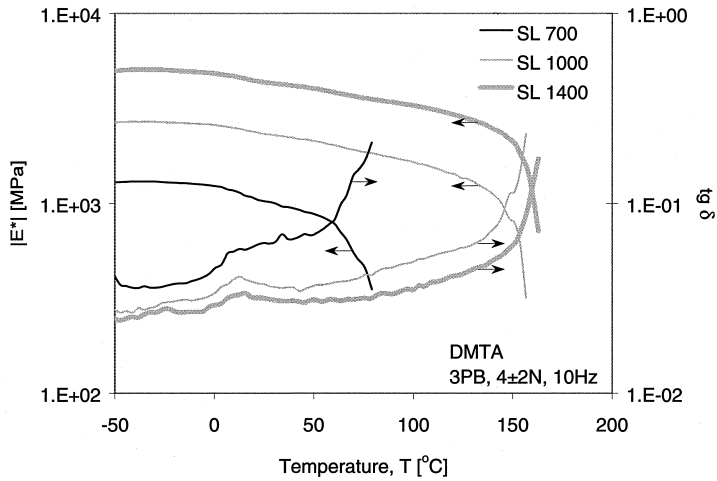

Fig. 3: Characteristic E^* and tgδ vs. T traces for the SL sheets of various surface weights.

3.2. In-Plane Static Loading

Crack Tip – Damage Zone Relation

Linear Elastic Fracture Mechanics (LEFM) offers easy-to-calculate and still meaningful measures of structural integrity even for materials being strictly speaking out of the scope of LEFM. In case of disordered fibrous materials prone to inelastic deformations there are, however, specific difficulties associated with uncertainty of crack tip position due to severe material damage combined with stress relieve in the damage zone. Nevertheless, there are analogies between LEFM and damage mechanics: (a) an ideal crack is a special case of damage with infinitely small damage zone, and (b) the toughness is the energy release rate per unit length movement of the entire damage zone. In this paper the authors benefited from the above analogies. Thus a certain *characteristic point* was rendered to an idealized crack *tip*, which moved parallel with the damage zone. This *characteristic point* was assigned to the located AE peak as defined in section *2.2*.

Fracture Behavior

The arranged sequence of AE peaks yielded a continuous trace over the ligament of the SEN-T specimen. This trace is compared with an actual crack pattern in Fig. 4. This picture demonstrates some systematic error in the crack location. This error may be attributed to

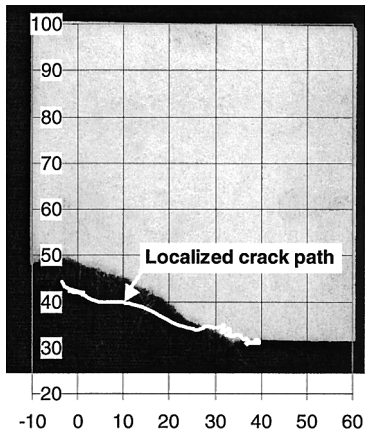

Fig. 4: Comparison of an actual crack pattern with a located AE peak trace in a SEN-T specimen of SL 1400. Note: each point of the path is the weight center of the located AE energy in a given time interval; coordinate axes in mm.

inhomogeneity and anisotropy of the sheets affecting the elastic wave propagation that has been used for location. Further, the movement of the upper two sensors (which were assumed as fixed, cf. Fig. 2) due to crack opening and peculiarities in the failure mode (long range pull-out; see later) may be of relevance.

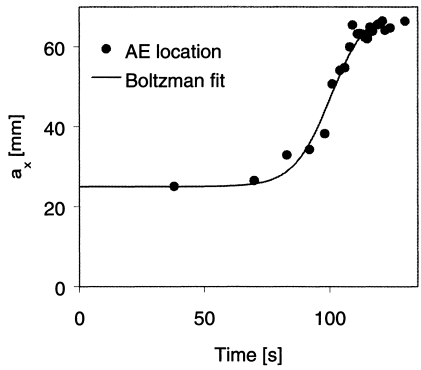

Fig. 5: Fitting of a located crack path with a Boltzman function (SL 700).

To follow the damage zone propagation the x projection of AE peak position $a_x \subset [a_0, W]$ was considered at the first approximation and inclination of the actual crack from that of the notch was neglected. If the located AE peak positions are well arranged in time a smooth curve appears for which a direct interpolation is feasible. If there are too few points or the scattering is too large (as in case of SL 700 depicted in Fig. 5) an additional fitting procedure should be applied. The authors used a Boltzman sigmoidal function to fit the a_x vs. time trace (cf. Fig. 5). By this way, the movement of the AE peak was "reconstructed" and several important characteristics, such as the resistance curve behavior, could be considered.

K_I resistance curves are depicted in Fig. 6. Here, K_I values were calculated according to Equation (1) by replacing maximum force with the actual one and the initial crack length with

the a_x values. The critical stress intensity factor (K_{IC}) was defined by the intersection of two linear trend lines drawn to the initiation and propagation regions. Results showed that K_Q, previously calculated from the maximum force, overestimated the critical stress intensity K_{IC} by about 20 %. This overestimation can be reasoned in the following way. At the maximum of the load–displacement diagram the load increase needed to expand the damage zone equals to the load decrement caused by weakening of the cross-section (resistance loss due to damage). Since in the early loading stage damage growth may already be superimposed to the propagation, the K_Q value was likely related to an underestimated flaw size.

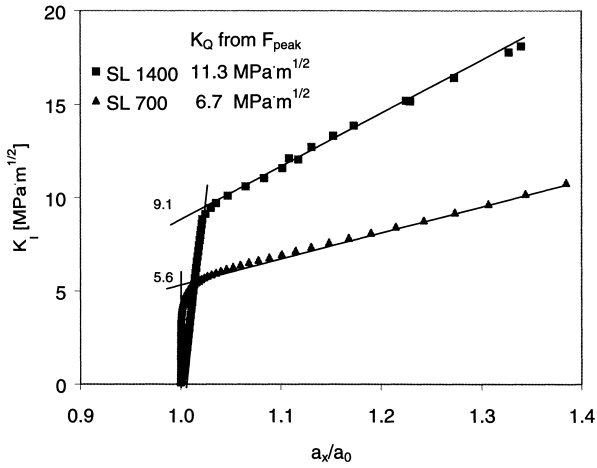

Fig. 6: Comparison of K_I resistance curves for SEN-T specimens of SL700 and SL1400.

Besides, the presented approach suggests a challenging possibility to follow the damage growth in material–related coordinate system (related to damage zone propagation path) instead of a geometry dependent load-deflection reference frame. The direct estimation of the energy release rate for comparison purpose or in absolute value (once AE energy is calibrated or related to mechanical energy) becomes very attractive. For an interval where the damage zone (DZ) propagation speed (given constant damage zone size) equals to that of the AE peak movement

$$\frac{da_{DZ}}{dt} = \frac{da_{AE}}{dt} \tag{6}$$

direct substitution is possible which would yield strain energy release rates

$$J = \frac{dE}{da_{DZ}} = \frac{dE}{da_{AE}}. \tag{7}$$

The same, naturally, should be true for the IT location method. Analysis of Fig. 7 shows that there is an interval [1.5…2.5] of relative AE peak position a_x/a_0 in which damage zone propagates in a steady state manner. The effect of the surface weight on the AE energy rate (slope of the related curve) is not so obvious however. It is not even constant showing for example two distinct slopes for SL 700 (cf. Fig. 7). By contrast, the absolute energy is affected much more. A future comparative study of AE and IT techniques would shed light on this aspect.

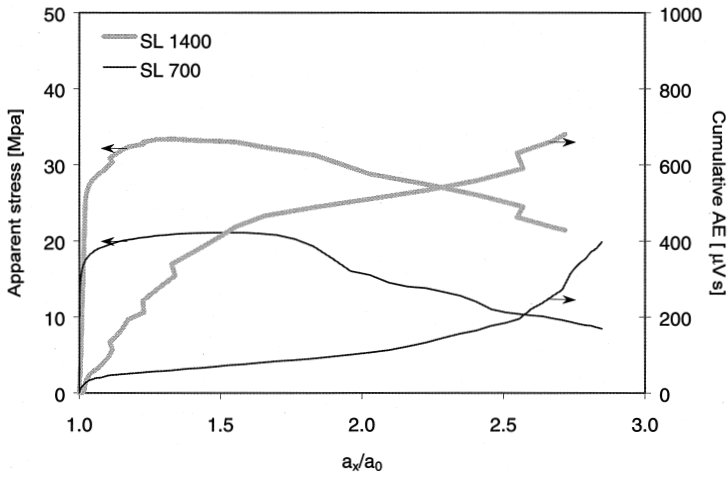

Fig. 7: Apparent stress and released AE energy versus AE peak position for SEN-T specimens.

Damage and Failure Assessment

Loading history of SEN-T specimens is depicted in Fig. 8. For convenience the AE data were grouped in two distinct stages: I – prior to maximum load and II – after the maximum load. This division roughly corresponds to the damage zone development (I), and propagation (II).

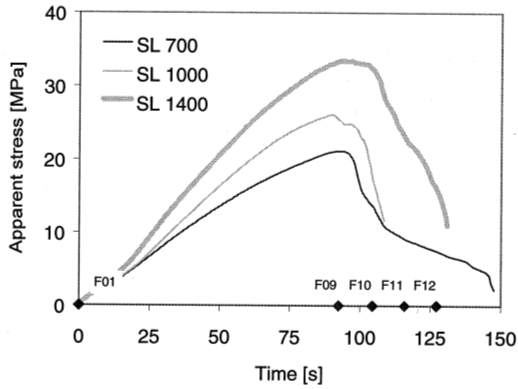

Fig. 8: Loading history for SEN-T specimens of various surface weights showing the sampling of the IT frames. Note: apparent stress calculated by dividing the tensile force with the initial cross-section of the free ligament.

Location of AE events (Fig. 9) of SL 700 tends to be less scattered as compared with SL 1400 for both for stages I and II. Damage zone size yields approximately 10 and 15 mm in the propagation stage for SL 700 and SL 1400, respectively, defined by the width of the related "damage band". An interesting detail is that in all cases the damage zone size in stage I is at least 1.5 larger than that of stage II. The former may be called static, while the latter cinematic damage zone size. Post-mortem inspection of the SEN-T specimens showed that the dominant failure is fiber pull-out. The pull-out length of the GF was closely matched to its initial length (12 mm). It is worth noting that the pull-out length of fully consolidated, well-bonded GF/PP composites is even less than 1 mm when the pull-out length is equaled with the half of the critical length value[9-10].

An example of the cumulative AE energy mapped in the zoomed window (cf. Fig. 2) in ***xy*** coordinate system over the entire fracture process is depicted in Fig. 10. The highest AE energy release can be seen near to the notch (left hand side). The absolute amount of this energy may depend on the parameters[11] others than the surface weight of the SL. About 5-7 mm wide crack propagation band is clearly distinguished in the middle of the investigated window. At the end of the band the AE intensifies due to the abrupt rupture of the specimen at final fracture.

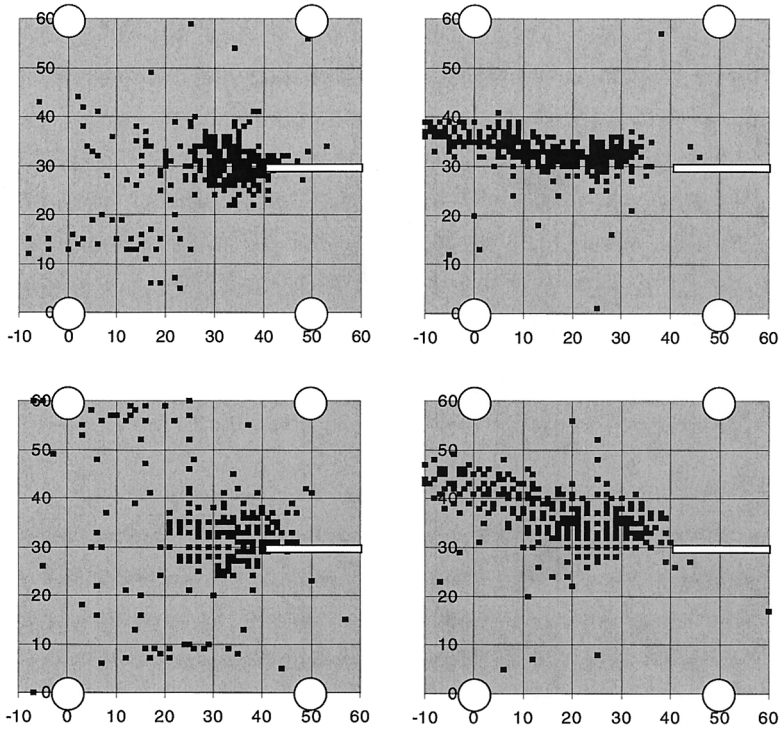

Fig. 9: Location of the AE events up to the maximum load (left) and after the maximum load (right) in a SEN-T specimen of SL 700 (upper) SL 1400 (lower). Note: coordinate axes in mm.

Fig. 11 compares the heat development in the same zoomed window for SL 700 and SL 1400 specimens. One can recognize the crack advance along the free ligament. The heat release in SL 1400 is superior to SL 700, which indicates for higher fracture toughness (and thus energy release rate) in accordance with the previous results. In analogy with the AE energy release in Fig. 7 the heat energy release rate can be estimated directly provided that the heat loss during the test can be determined. Further, one can assume that the mechanical energy release rate (J_c) is proportional (or even equal) with that of the heat. This aspect should be checked in the future.

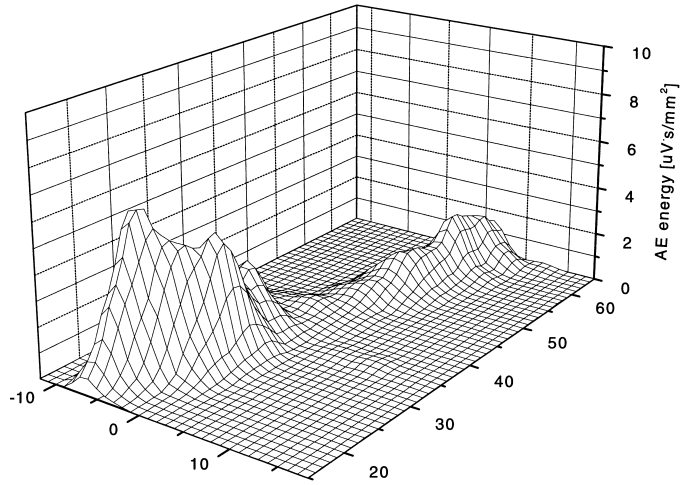

Fig. 10: Mapping of the localized cumulative AE energy of the entire fracture process in a SEN-T specimen of SL 1400.

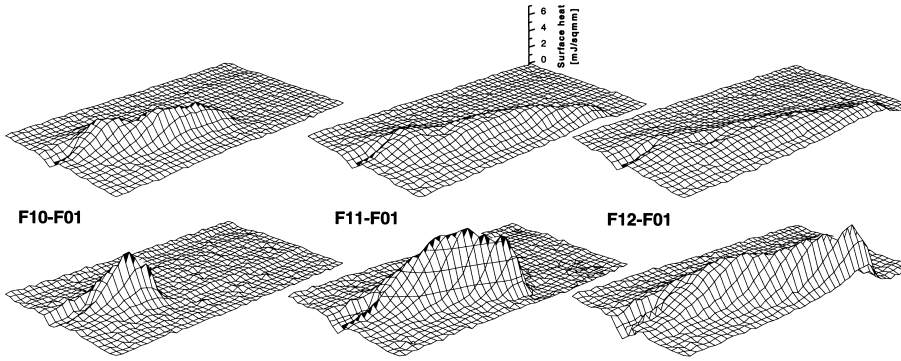

Fig. 11: 3D contour plots of the surface heat energy release during crack growth. Designations: upper and lower rows SL 700 and SL 1400 respectively.

3.3. Out-of-Plane Dynamic Loading

Fig. 12 compares characteristic force- and energy-deflection IFWI traces of the SL sheets with various surface weights. One can recognize that F_{peak} and E_{tot} steeply increase with increasing density. The same note holds for the stress at the maximum load (cf. Table 1). Moreover, all load-, stress- and energy-related IFWI parameters show a linear increase as a

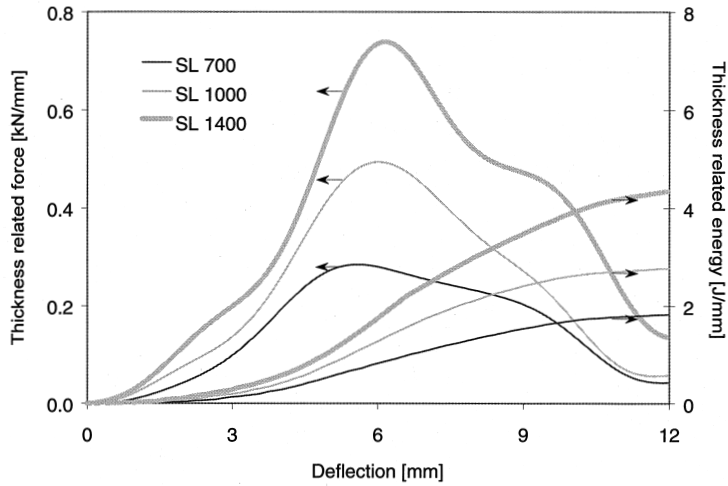

Fig. 12: Characteristic force- and energy-deflection IFWI traces of the SL sheets with various surface weights.

function of the surface weight or density. The deflection values at maximum load and full perforation (X_{peak}, X_{tot} respectively) are practically the same. In addition, the DI values showed also no variation with the density. One can thus conclude that similar failure events were at work in all SL samples. So, our above claim that all force- and energy-related terms are solely dependent on the sheet density seems to be corroborated.

Table 1. Results from the instrumented falling weight impact (IFWI) tests. Designation: t – thickness (=2 mm).

Sample	Density	F_{peak}/t	E_{peak}/t	X_{peak}	σ_{peak}	E_{tot}/t	X_{tot}	DI
	$g \cdot m^{-3}$	$kN \cdot mm^{-1}$	$J \cdot mm^{-1}$	mm	MPa	$J \cdot mm^{-1}$	mm	-
SL 700	0.35	0.3	0.8	5.7	172	2.0	11.8	0.60
SL 1000	0.50	0.5	1.1	6.0	263	3.0	12.0	0.62
SL 1400	0.70	0.8	2.1	6.1	405	4.9	12.5	0.58

4. Conclusions

Based on this study performed on the in-plane static and out-of-plane dynamic fracture and related failure behavior of partially consolidated discontinuous glass fiber (GF) mat-

reinforced polypropylene (PP) composites (Azdel SuperLite®, SL), the following conclusions can be drawn:

- the crack path can be reliably estimated by considering the time dependence of the located AE activity, viz. via the change of the gravity of the cumulative AE energy. By this way the fracture performance can be studied in a material-related coordinate system and even the crack resistance curve can be determined. The latter allows us to conclude the initiation fracture toughness value;
- locating the AE and mapping the heat rise by means of infrared thermography (IT) the size of the damage zone can be estimated. Its size was larger in the crack initiation compared to the crack propagation stage. It was suggested that the energy release rate can be determined directly by considering, the located AE or IT or by their combination;
- the failure mechanism is dominated by pull-out along with some fiber fracture. Note that partial consolidation caused considerably longer fiber pull-out compared to fully consolidated types. This may require the revision of the pull-out concept.
- all stress- and energy related characteristic terms under perforation impact conditions are solely dependent on the density (surface weight) of the SL sheets. These parameters change linearly with the density in the first approximation.

Acknowledgements

The authors are thankful to Dr. H. Dittmar for the delivery of the Azdel SuperLite® sheets. Part of this work was performed in the framework of a DFG project.

References

[1] J.Jansz in *Polypropylene: An A-Z Reference*, J.Karger-Kocsis (Ed.), Kluwer, Dordrecht, 1999, p.643
[2] J.Karger-Kocsis, *Polym.Compos.*, **21**, 514 (2000)
[3] D.M.Bigg in *Polypropylene: Structure, Blends and Composites*, Vol.3 Composites, J.Karger-Kocsis (Ed.), Chapman and Hall, London, 1995, p. 263
[4] L.A.Berglund and M.L.Ericson in *Polypropylene: Structure, Blends and Composites*, Vol.3 Composites, J.Karger-Kocsis (Ed.), Chapman and Hall, London, p. 202
[5] H.Dittmar, J.Groen, F.Mooijman and C.Peterson in *Langfaserverstärkte Thermoplaste im Automobil – Stand der Technik und zukünftige Perspektiven*, Würzburg, 9-10 Oct. 1999, SKZ, Würzburg, 1999, p. C/2
[6] T.L.Anderson *Fracture Mechanics: Fundamentals and Applications*, CRC Press, 1995, p. 606
[7] M.Jirásek, *Int. J. Solids & Structures*, **35**, 4133 (1998)
[8] O.I.Benevolenski, K.-P.Mieck, T.Reußmann and J.Karger-Kocsis, *J. Thermoplast. Compos. Mater.*, 13, 481 (2000)
[9] J.Karger-Kocsis, K. Friedrich and R.S.Bailey, *Adv. Compos. Mater.* **1**, 103 (1991)
[10] S.-Y.Fu, B.Lauke, E.Mäder, C.-Y.Yue, X. Hu, *Composites: Part A* **31**, 1117 (2000)
[11] O.I.Benevolenski, Gy.Krállics, *Proceedings of First Conference on Mechanical Engineering*, K.Molnár, Gy.Ziaja and G.Vörös (Eds.), Springer-Verlag, Budapest, vol. 1, 22, (1998)